Experimental Results from an Antineutrino Detector for Cooperative Monitoring of Nuclear Reactors

N. S. Bowden [a,*], A. Bernstein [b], M. Allen [a], J. S. Brennan [a], M. Cunningham [b], J. K. Estrada [a], C. M. R. Greaves [a,1], C. Hagmann [b], J. Lund [a], W. Mengesha [a], T. D. Weinbeck [a,2], C. D. Winant [b]

[a] *Sandia National Laboratories, Livermore, CA 94550, USA*

[b] *Lawrence Livermore National Laboratory, Livermore, CA 94550, USA*

Abstract

Our collaboration has designed, installed, and operated a compact antineutrino detector at a nuclear power station, for the purpose of monitoring the power and plutonium content of the reactor core. This paper focuses on the basic properties and performance of the detector. We describe the site, the reactor source, and the detector, and provide data that clearly show the expected antineutrino signal. Our data and experience demonstrate that it is possible to operate a simple, relatively small, antineutrino detector near a reactor, in a non-intrusive and unattended mode for months to years at a time, from outside the reactor containment, with no disruption of day-to-day operations at the reactor site. This unique real-time cooperative monitoring capability may be of interest for the International Atomic Energy Agency (IAEA) reactor safeguards program and similar regimes.

Key words: nuclear reactor safeguards; antineutrino detection; Gadolinium loaded liquid scintillator
PACS: 89.30.Gg, 28.41.-i

* Corresponding Author. Tel.: +1 925 294 2566.
Email address: nbowden@sandia.gov (N. S. Bowden).

[1] Present Address: Lawrence Berkeley National Laboratory, Berkeley, CA 94720, USA

[2] Present Address: Department of Physics and Astronomy, Tufts University, Medford, MA 02155, USA

1 Introduction

The IAEA uses an ensemble of procedures and technologies, collectively referred to as the Safeguards Regime, to detect diversion of fissile materials from civil nuclear fuel cycle facilities into weapons programs. The research described here concerns safeguards for one important element of this cycle, nuclear reactors. Earlier work [1,2] has described a method for exploiting the large number ($\approx 10^{21}$ $\bar{\nu}$/s) of antineutrinos emitted by fission reactors to track the plutonium content and thermal power of the reactor core in real time. This approach offers unique advantages that are complimentary to existing safeguards methods. The potential impact on the regime is large, inasmuch as over 200 of the world's civil power reactors, located in some 30 countries, are subject to IAEA safeguards [3].

To be useful for reactor safeguards, antineutrino detectors must be simpler to construct and operate than the current generation of detectors, which were built to investigate the basic physics of the neutrino sector. It is in this respect that this work differs from the experimental effort described in [1]. Furthermore, an experimental deployment at a commercial reactor is essential to demonstrate the potential of this technology to the global non-proliferation community.

In this paper, we describe the characteristics and performance of such a device; a simple, compact prototype antineutrino detector, "SONGS1", which has been installed at a commercial nuclear power station to demonstrate the feasibility of this monitoring technique.

2 Reactor Monitoring with Antineutrino Detectors

In the context of nuclear nonproliferation, cooperative monitoring refers to the tracking of nuclear inventories and nuclear facilities with the agreement of the host country. The IAEA Safeguards Regime is the most prominent example of such monitoring. Antineutrinos have unique features that make them interesting for the purpose of cooperative monitoring of nuclear reactors. The highly penetrating nature of the particle and the high flux near reactors means that relatively small detectors external to the reactor can acquire a signal useful for monitoring, even with hour to day integration times. Furthermore, over a broad range of antineutrino energies, the ratio of antineutrinos per fission and MeV emitted by uranium and plutonium varies by factors of 50–90% [4]. As a result, as uranium is consumed and plutonium produced in the core, the measured antineutrino rate and spectrum will change, providing up to date information about the burnup and isotopic content of the core.

For example, during a typical 1–1.5 year cycle at a pressurized water reactor (PWR), the net effect on the antineutrino rate due to the fissile isotopic evolution is 6–12%. Information about the reactor's fissile content is a key element of the IAEA safeguards regime, whose purpose is to detect unauthorized diversion of fissile material from civil nuclear fuel cycles. Antineutrino detectors can supply this information in real time and in a manner wholly under the control of the safeguards agent, without interfering with daily reactor operations. Because of these interesting features, antineutrino detection holds promise as a complementary technique for IAEA and other reactor safeguards regimes.

2.1 Relative and Absolute Measurements

In neutrino physics experiments that require an absolute flux or spectral measurement, considerable effort must be devoted to a full understanding of the absolute efficiency of the detector. In safeguards regimes, both relative and absolute measurements may be of use. Relative measurements, in which the antineutrino rate or spectrum is compared to some initial value, are insensitive to time-independent systematic shifts in the detector response, such as an error in an estimate of the detection efficiency. For such measurements, a detailed understanding of the individual detector's efficiency is therefore not required, so long as the detector response is stable in time. In the analysis presented here, we have estimated the efficiency of the SONGS1 detector using a simple detector simulation. We emphasize that the potential utility of the detector for safeguards does not depend on a precise knowledge of this efficiency.

3 Site and Reactor Characteristics

The SONGS1 detector is deployed at Unit 2 of the San Onofre Nuclear Generating Station (SONGS). There are two operational reactors at this station; both are pressurized water reactors designed by Combustion Engineering in the 1970s and have maximum thermal (electric) power of 3.4 GW_{th} (1.1 GW_{elec}).

The detector is located in the tendon gallery of Unit 2 (Fig. 1). A feature of many commercial reactors [5,6,7,8,9], a tendon gallery is an annular concrete hall that lies beneath the walls of the reactor containment structure. It is used to inspect and adjust the tension in reinforcing steel cables which extend throughout the concrete of the containment structure. At SONGS these inspections occur every two to three years, and involve the examination of only a

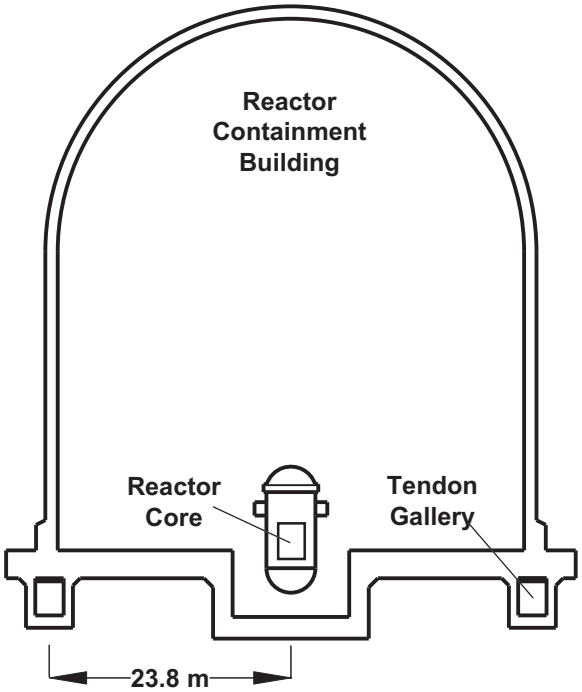

Fig. 1. A cross section of the SONGS Unit 2 containment building showing the position of the reactor vessel and tendon gallery.

handful of representative tendons. Subsequently, the placement of the detector in the tendon gallery has little or no impact on regular plant operations.

SONGS1 is located 24.5 ± 1.0 m from the Unit 2 reactor core and 149 ± 3 m from that of Unit 3. Since the antineutrino flux generated by each core is isotropic, 97% of the reactor antineutrinos reaching the SONGS1 detector originate from Unit 2. With Unit 2 at full power the antineutrino flux at the SONGS1 location is $\approx 10^{17}$ $\mathrm{m^{-2}s^{-1}}$.

It is worth noting that at this position the flux of other particles, in particular fast neutrons and gamma rays, reaching the detector from the reactor core is practically zero. For example, the material between the core and the detector corresponds to nearly 100 attenuation lengths for 10 MeV neutrons, compared with a total flux exiting the reactor that is no greater than 10^8 $\mathrm{cm^2s^{-1}}$. This yields a vanishingly small reactor neutron flux in the gallery. Similar arguments apply for reactor produced gamma rays.

The tendon gallery is located about 10 m below the surface, providing $\approx$ 25 meters of water equivalent (mwe) overburden which eliminates the soft component of the cosmic ray flux and reduces the muonic component by a factor of 7 [10]. An important purpose of this prototype deployment was to determine whether cosmic ray induced backgrounds at this relatively shallow depth would overwhelm the reactor antineutrino signal in a simple detector.

The temperature in the tendon gallery is not actively controlled. Due to the underground location diurnal temperature variations at the detector are small (< 0.1 °C), although there is a slow seasonal variation of up to 5 °C. Small drifts in detector gain that result from this variation are accounted for via the detector calibration procedure (Sec. 9).

In the context of cooperative monitoring, tendon galleries are ideal locations for antineutrino detectors. They are remote from daily reactor operations, provide significant overburden, and are as close as possible to the core while remaining outside of containment.

4 Antineutrino Interactions in Liquid Scintillator

Antineutrinos are detected via the inverse beta decay process on quasi-free protons in hydrogenous scintillator: $\bar{\nu}_e + p \rightarrow e^+ + n$. The positron ($e^+$) and neutron ($n$) are detected in close time coincidence, allowing strong rejection of the much more frequent singles backgrounds due to natural radioactivity or neutron production. The positron deposits energy via Bethe-Bloch ionization as it slows in the scintillator, and upon annihilation with an electron, emits two gamma rays which can deposit up to an additional 1.022 MeV of energy. Because the ionization and annihilation gamma ray energy depositions are effectively simultaneous, and promptly follow the antineutrino interaction, this combination of energy depositions is measured as a single event in the detector, referred to as the "prompt" energy deposition. Assuming complete containment of the event, the prompt energy and the antineutrino energy are directly related through the equation:

$$E_\nu = E_{prompt} + 1.8\ MeV - 2 \cdot m_e. \tag{1}$$

In the current detector, this ideal relation is distorted by escape of 0.511 MeV annihilation gamma rays that are created near the edge of the detector. Monte Carlo transport simulations account for this loss of energy, and allow for a full analysis of the deposited energy spectrum as well as providing an estimate of the efficiency for detection of the prompt energy (Sec. 8.4).

The neutron carries away a few keV of energy from the antineutrino interaction [11] and is detected by capture on a Gadolinium (Gd) dopant. The liquid scintillator is doped at 0.1% by weight with natural Gd, which is chosen for its very high neutron capture cross-section. The Gd doping yields a neutron capture time of 28 μs and an energy release of ≈ 8 MeV via a gamma ray cascade, compared to a capture time of 200 μs and energy release of 2.2 MeV for capture on hydrogen. The interactions in the detector resulting

from this 8 MeV cascade are referred to as the "delayed" energy deposition. As with the positron, the measured energy in the detector is somewhat less than 8 MeV since some of the cascade gamma rays escape the detector volume without depositing their full energy. Still, the increase in deposited energy and the decrease in the time interval combine to significantly improve the overall background rejection capability relative to capture in undoped scintillator.

We can therefore expect to observe two classes of events in a detector based upon Gd loaded liquid scintillator. The first, referred to here as correlated events, involve a prompt energy deposition associated with a neutron that is captured a short time later on a Gd nucleus. The time separation between prompt and delayed energy depositions will follow an exponential distribution with time constant equal to the neutron capture time of the Gd doped scintillator (28 μs). The second class, referred to as uncorrelated backgrounds, involves the random "coincidence" of two independent energy depositions caused by natural backgrounds. We refer to these individual energy depositions as "singles." Since these backgrounds obey Poisson statistics, the time separation between singles will also follow an exponential distribution with time constant equal to the inverse of the singles rate (effectively the detector trigger rate).

Unfortunately, antineutrino interactions are not the only events that produce correlated events in the detector. For example, fast neutrons, produced by muon capture or muon spallation [12,13,14], can scatter off protons in the scintillator, giving a prompt energy deposition, and then be captured on Gd with the characteristic time distribution. Therefore, observation of correlated events alone is not sufficient to measure the reactor antineutrino flux – the correlated background rate must also be determined. Accurate *a priori* calculations of the background are difficult since they depend strongly upon the geometry and composition of the detector surroundings. In practice, one must wait for a reactor off period to measure the correlated background rate.

5 SONGS1 Detector Description

The SONGS1 detector consists of three subsystems; a central detector containing the Gd-doped liquid scintillator target and photomultiplier tubes, a passive water or polyethylene shield on all sides, and a plastic scintillator muon veto system placed outside the water shield on five sides of the detector.

In addition to the detector itself the installation at SONGS includes the Data Acquisition System (DAQ, Sec. 7) and a computer that automatically performs the data analysis described in Sec. 10. A modem is used to automatically retrieve the results of this analysis as well as detector state of health

indicators, allowing for the remote monitoring of the detector, and indeed of reactor operation. The SONGS1 system typically operates without physical intervention for months at a time.

5.1 Central detector

The central detector, seen in Fig. 2, consists of four identical stainless steel cells, each with inner dimensions of $\approx$ 43 cm by $\approx$ 43 cm by $\approx$ 98 cm, filled with $\approx$ 0.64 tons of liquid scintillator. Stainless steel was used rather than the more typical acrylic to avoid any possibility of attack by the scintillator on the container walls, and subsequent leakage of the flammable scintillator. To improve reflectivity, the sides and bottom of each cell are lined with foil wrapped acrylic sheets. To increase the fraction of totally internally reflected (TIR) light, these sheets were sealed within transparent FluorinatedEthylene-Propylene (FEP) bags filled with Argon [15]. The bags make it difficult to measure the detector volume to high precision, resulting in a $\approx$ 10% uncertainty in this quantity. However, this is of no consequence for our relative measurement of the reactor antineutrino flux.

We use scintillator remaining after the completion of the Palo Verde antineutrino detection experiment [16]. This scintillator has a density of 0.856 g cm^{-3} and is 13% hydrogen by weight. The development and characteristics of this scintillator are described in detail elsewhere [17].

Scintillation light generated by the interaction of particles in the cells propagates to 9 inch hemispherical Photonis XP1802 photomultiplier tubes (PMTs) by means of an acrylic coupling cylinder submerged in the liquid and extending through an opaque acrylic lid. There are two PMTs mounted on each cell (not shown in Fig. 2).

5.2 Passive Shielding

Both gamma ray and neutron fluxes in the central detector are reduced by passive water or polyethylene shielding which surrounds the detector on six sides. The water is contained in acrylic tanks, supported by perforated angle stainless steel racks. On average the passive layer is $\approx$ 0.5 m thick. An MCNP simulation predicts that a shield of this thickness reduces the flux of 10 MeV neutrons and 2 MeV gamma rays by factors of 25 and 10 respectively.

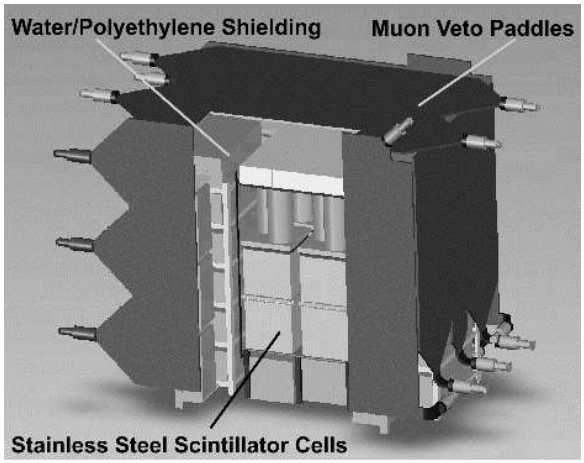

Fig. 2. A cut away diagram of the SONGS1 detector, showing the major subsystems.

5.3 Muon Veto

A 2 cm thick plastic scintillator envelope identifies and rejects cosmic ray muons. As shown in Fig. 2, the envelope is comprised of scintillator paddles of different sizes placed on five sides of the detector, read out by photomultiplier tubes. The paddles are wrapped first with aluminum foil to enhance reflectivity and then with black tape for light tightness.

For the top, horizontally oriented paddles, the well separated muon peak was identified in the paddle energy distribution, at its expected location of 5 MeV. The energy threshold defining a muon was set three sigma below this peak, with the sigma defined by a fit to the rising lobe of the Landau-distributed muon spectrum. This procedure introduces a small amount of contamination from the tail of the paddle gamma ray distribution, which extends above 3 MeV, but the total deadtime introduced by the muon veto even with this contamination remains small. Due to the geometry of muon interactions, the muon spectrum in the vertically oriented paddles has no clear peak. Thresholds in vertically oriented paddles were set relative to the rates in the horizontal paddles, by assuming a $cos^2(\theta)$ distribution for the muon flux, which predicts that the flux through a vertically oriented paddle should be 50% that of a horizontally oriented paddle. The total rate at which muons are recorded by this system is $\approx$ 500 Hz.

6 Expected Antineutrino Rates

The number of detected antineutrino interactions in the detector is directly related to the individual isotopic fission rates through the equation

$$N_{\bar{\nu}} = \left(\frac{TN_p}{4\pi D^2}\right) \sum_i f_i \int dE_{\bar{\nu}} \sigma(E_{\bar{\nu}}) \phi_i(E_{\bar{\nu}}) \epsilon(E_{\bar{\nu}}). \quad (2)$$

In this equation, $N_{\bar{\nu}}$ is the number of detected antineutrino interactions in a time interval T. N_p is the number of target protons in the detector, D is the distance from the detector to the center of the reactor core, f_i is the number of fissions per second from the ith isotope. In practice the index runs over the four dominant fissioning isotopes ^{235}U, ^{238}U, ^{239}Pu and ^{241}Pu, which account for $\approx 99.9\%$ of fissions in a typical reactor. σ and ϕ_i, both depending on the antineutrino energy $E_{\bar{\nu}}$, are respectively the cross-section for the inverse beta interaction, and the number density per MeV and fission for the ith isotope. ϵ is the energy dependent intrinsic detection efficiency. The integral extends over all antineutrino energies above the 1.8 MeV threshold of the inverse beta interaction.

With our current 0.64 ± 0.06 ton liquid scintillator detector at a standoff of 24.5 ± 1 m from the reactor core, and with the reactor parameters defined in Sec. 3, the rate predicted by Eq. 2 at the beginning of the reactor fuel cycle is approximately 3800 ± 440 antineutrino interactions per day for a perfectly efficient detector.

7 Electronics and Data Acquisition System

Fig. 3 shows the architecture of the data acquisition and trigger. As mentioned earlier, there are two PMTs per scintillator cell. Custom preamplifiers built into the bases of the PMTs produce tail pulses that are sent to a CAEN N568 spectroscopy amplifier for shaping. The approximately Gaussian shaped output of the N568 is passed directly to two CAEN V785 peak sensing Analog-to-Digital-Converters (ADCs).

A fast amplified signal from the N568 amplifier is passed to a CAEN V812 Constant Fraction Discriminator (CFD) module. Hardware thresholds are set at ≈ 1.5 MeV for each PMT, so as to allow online calibration using the 2.6 MeV ^{208}Tl gamma ray from the Thorium chain (Sec 9).

The anode outputs of all muon paddles are passed directly to CAEN V812 CFDs, and the OR output from these is used for vetoing and timing purposes.

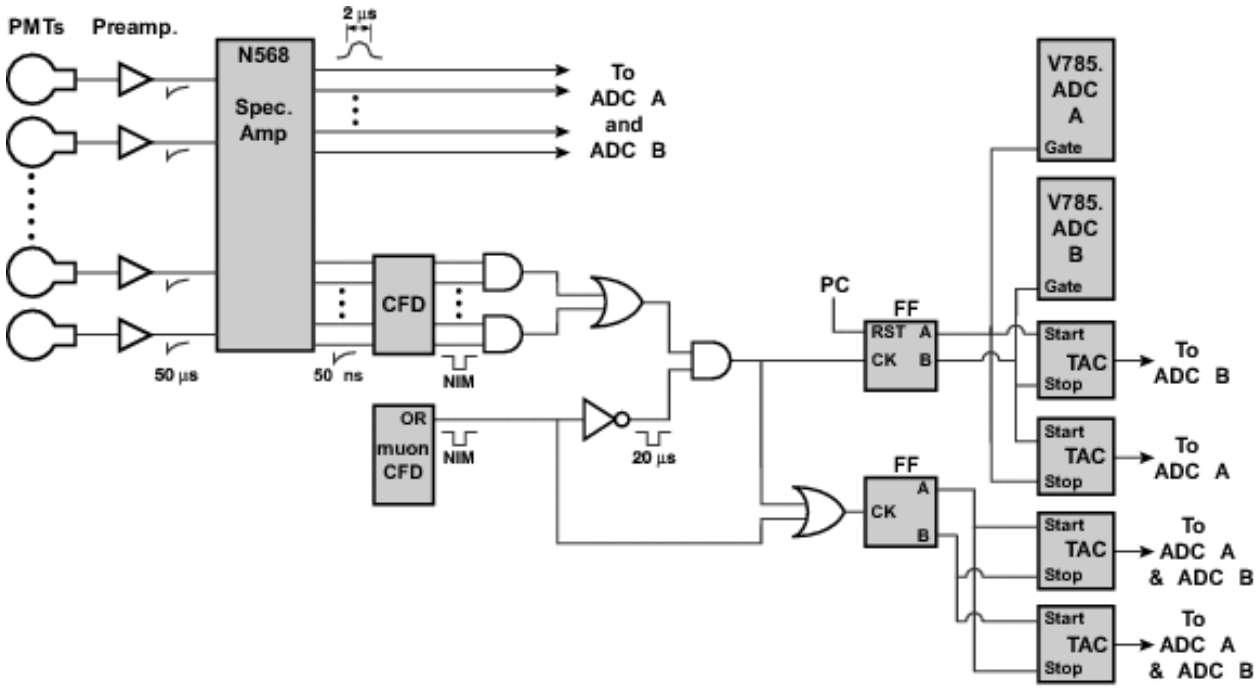

Fig. 3. The data acquisition system and trigger logic.

Gates for the ADCs are produced by the following trigger logic. A coincidence is formed from the two discriminator outputs corresponding to the PMTs on the same cell using an ORTEC C4020 logic module (a cell trigger – typically 120 Hz per cell). The logical OR of the four cell triggers is taken (typically 500 Hz), and combined with the logical NOT of a 20 μs long muon veto signal. A non-retriggerable logic pulse of 3 μs duration (an acquisition trigger – typical rate 420 Hz) is produced at this stage since this is the approximate duration of the shaped output of the N568; accepting events with shorter separation would only result in pulse pileup at the ADCs.

Thus, an event that causes two PMTs from any single cell to fire in coincidence, at least 20 μs after the passage of the last muon and 3 μs after the last cell trigger, will result in one of the ADCs being gated. Gates are generated for each ADC in turn, so that while one ADC is digitizing (V785 digitization time $\approx$ 6 μs) the other can accept another event. Gates are generated until the 32 event buffer on each ADC is full. Once these buffers have been emptied, the flip flop generating the alternating gates is reset so that it is known which ADC receives the first trigger, allowing subsequent events to be formed into correctly ordered pairs in later analysis (Sec. 10).

In similar fashion, pairs of Time-to-Amplitude-Converters (TACs) are used to record timing information. The ORTEC 566 TACs utilized have a long 50 μs reset time, which if used singly would result in an unacceptably large fraction of events being recorded without timing information. Thus, start and stop signals are alternated between a pair of TACs; the stop for one is the start for

the other. To record the time between pairs of events (the interevent time) the acquisition trigger serves as both the start and the stop signal. To be certain that the combination of ADC and TAC deadtimes does not introduce a non-uniform response, we only consider interevent times greater than 10 μs in the analysis that follows.

To record the time to last muon, the acquisition trigger serves as the stop signal, while the start signal is either the previous acquisition trigger or a muon signal if that occurred sooner. This start logic is necessary since the TACs are single shot – the production of a TAC output pulse clears the timer. Always recording the time to last event, either muon or cell, solves this problem, but introduces about 4% extra deadtime. Both TAC signals are digitized simultaneously with the PMT pulses by the peak sensing ADCs.

8 Detector Simulation

A high fidelity detector simulation is not necessary for the relative antineutrino rate measurements of interest here. Indeed, this lack of reliance on simulation is a strength in the context of the practical application of antineutrino detection technology to safeguards. Instead, we used Monte Carlo simulations to gain insight into the atypical particle transport properties of the SONGS1 detector, and to estimate the efficiency of our detector.

We used the MCNPX [18] package, which simulates particle transport, but does not model the transport of the optical photons generated in the scintillation process. To account for the optical photon response, we used a simple model that incorporates photostatistics and the measured vertical position variation in each cell. Because the variation in light collection has an important effect on the response function, a fuller understanding of the detector response ultimately requires a simulation or measurement of the transport properties of visible scintillation photons throughout the entire detector volume. However, even without these inputs, we can still estimate the energy scale and the positron and neutron detection efficiencies, and confirm the expected transport behavior of positrons, neutrons and gamma rays in the detector and surrounding materials.

8.1 The Detector Simulation in MCNP

We simulated particle transport in the scintillator, the surrounding materials including the acrylic optical couplings, the PMTs, the reflective panels inside the detector, the stainless steel detector walls and support structure, the

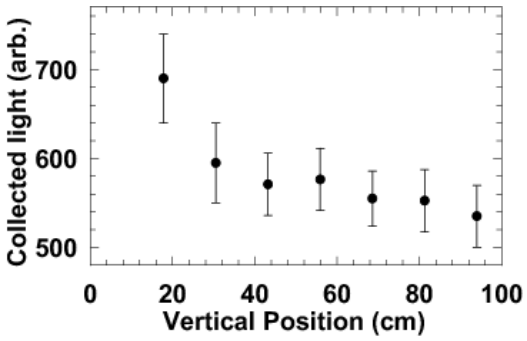

Fig. 4. The average PMT response as a function of vertical position in a single cell. The position is measured with respect to the top of the cell.

water shield and the plastic muon veto. Characteristic gamma rays for the background simulation (Sec. 8.3) were propagated from a maximum depth of 0.5 m in the surrounding concrete – beyond this depth there was a negligible chance for interaction in the detector.

8.2 The Vertical LED Scan and the Detector Optical Model

Partial characterization of the optical response of the detector was derived from a vertical scan in one cell with a light emitting diode (LED). The LED position was offset approximately 8 centimeters transversely from the center of the cell. Pulse height spectra were recorded at seven positions from 10 to 90 cm from the top of the scintillator cell. The variation in response, averaged over the two PMTs, is plotted in Fig. 4. As seen in the figure, the response is fairly uniform until the source is within about 20 cm of the top of the cell.

We use this data set to parameterize the effects of both photostatistics and vertical position on the detector energy resolution. The parametrization is then used to estimate the effect of optics on the energy resolution in the gamma ray, neutron, and positron transport simulations described below. We model the optical resolution function $\sigma_{opt}(E)$ as:

$$\sigma_{opt}(E) = \sigma_{pos}(E) + \sigma_{p.e.}(E) = k1 \cdot E + k2 \cdot \sqrt{E} \tag{3}$$

Here $\sigma_{pos}(E)$ represents the average effect of the vertical position on the PMT response, and $\sigma_{p.e.}(E)$ is the variation in response caused by the finite number of photoelectrons generated in the event. A value of 0.03 for $k1$ is estimated from the LED data in Fig. 4. $k2$, accounting for photostatistics, has a value of 0.15, which is the typical fractional width of the LED pulse hight spectra in the position scan.

Although horizontal variation of light collection has an important impact on

the resolution, a horizontal scan at different heights was impractical and was not included in the model. While this ultimately limits the fidelity of the simulation, this simple model is sufficient to estimate the energy scale and detection efficiencies, and confirms our main expectations about the detector response to antineutrino events.

8.3 Gamma-ray Energy Calibration

As described in Sec. 9 the detector energy calibration is derived from a fit to a spectral feature due to the 2.6 MeV ^{208}Tl gamma ray from the Thorium chain and to measured ADC pedestal values. This broad feature lies between the Tl photopeak and Compton edge, and arises from the multiple Compton interactions that a gamma ray is likely to undergo in the detector. The size of the detector is such that there is a high likelihood that a large fraction of the gamma ray energy will be lost within it. To estimate the average energy deposited by this process, and thus the correct energy to assign the measured position of this feature in our calibration process, we propagated gamma rays from natural Uranium (U), Thorium (Th) and Potassium (K) in external concrete through the detector components just described and into the active detector volume.

Gamma interactions from U, Th, and K are all generated independently, and a weighted sum of the resulting spectra is used to form the simulated total gamma-ray energy spectrum. In comparing data and Monte Carlo, the relative isotopic abundances of U, Th, and K are taken as free parameters, along with an overall scale factor. Smearing due to position and photostatistics is fixed by the optical model defined in Sec. 8.2. The four free parameters are optimized by fitting to the data in the 1 to 3 MeV gamma ray calibration energy range. The χ^2 per degree of freedom for the fit is 1.2.

Fig. 5 compares the data and Monte Carlo. Once agreement is optimized in the energy range of interest, the energy scale is set in the data by matching the measured ADC values of the multiple Compton scatter feature to the energies reported by the Monte Carlo. The inferred energy values for the K and Th lines are 1.32 and 2.39 MeV respectively.

Despite the absence of a full optical model, the simulation reproduces the main features of the data, namely the spectral features due to the multiple Compton scattering of K and Th gamma rays, and shows reasonable fidelity across the two orders of magnitude variation in the pulse height spectrum.

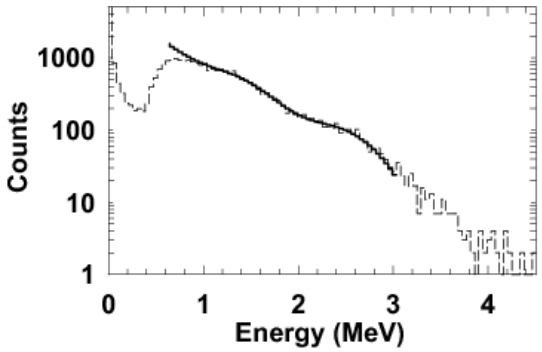

Fig. 5. External gamma interactions as recorded in the SONGS1 detector, compared with the MCNP simulation (solid line).

8.4 Positron Simulation

Antineutrino-generated positrons, with energies from zero to several MeV, travel a few centimeters from their point of creation and annihilate with the creation of two 511 keV gamma rays. We simulated positrons randomly distributed throughout the liquid scintillator volume, and tallied the total visible energy recorded in each cell, including the positron ionization energy, and the energy deposited by scattering of the annihilation gamma rays.

The positron energy distribution is directly related to the antineutrino energy distribution through Eq. 1 in Sec. 4. Because the positron energy spectrum changes as the reactor evolves, the simulated spectrum must be integrated over the same burnup period as the actual data. In the data presented here, this corresponds to the first 77 days of Cycle 14 of the SONGS reactor. The variation due to the changing isotopics in the core is correctly accounted for in our predicted spectrum.

Fig. 14(b) shows the simulated and measured positron spectra in our detector. The fixed parameters from the optical model are used to define the effects of position and photostatistics on the positron energy scale. The only free parameter is an overall normalization factor.

The distributions reveal agreement at approximately the 5 % level between data and the model. A fuller treatment of the optical response is required for a more precise comparison. We estimate a detection efficiency of $55\% \pm 5\%$ for antineutrino generated positrons in the prompt energy range of 2.39 to 9 MeV. The uncertainty is estimated by comparing the sum of the absolute magnitudes of bin to bin count variations between the data and Monte Carlo spectra with the total number of data counts in the prompt energy range.

8.5 Neutron Simulation

Neutrons from inverse beta decay within the liquid scintillator are created with energy of order 1 keV. Subsequent elastic collisions thermalize the neutrons until they are either captured or escape from the scintillator volume. With a natural Gd loading of 0.1% by weight, approximately 88% of neutron captures will be on Gd isotopes (^{155}Gd 82%, ^{157}Gd 18%), with the remainder capturing on protons.

The response of the detector to thermal neutrons generated by antineutrino interactions has an important effect on the overall efficiency. We simulated the gamma-ray cascade from neutron capture on Gd with the DICEBOX algorithm [19]. About 105 gamma cascades per isotope with an average multiplicity of ≈ 5 were calculated and written to a file. Our modified version of MCNPX read in a new set of energies whenever a capture on Gd occurred. The resulting gamma rays were then propagated isotropically from the final neutron position, tracked, and energy deposits were tallied for each detector cell. To estimate the efficiency for detection of neutrons from antineutrino interactions, the simulated neutrons were distributed uniformly throughout the active volume of the detector. Neutron energies were sampled from the energy distribution of antineutrino-generated neutrons, and allowed to thermalize and capture in the detector.

Fig. 12(b) shows a comparison of the data and Monte-Carlo, where the data are selected using all criteria that define an antineutrino, as presented in Sec. 10. As with the positron simulation, the only free parameter is an overall normalization constant.

Again, the agreement between data and Monte Carlo is reasonable considering the simplicity of the model. Qualitatively, the Monte Carlo confirms a key expectation for this type of detector: there is a broad range of energy depositions arising from the Gd capture, which extends well below the 8 MeV total energy of the gamma ray cascade. The peak near 2.2 MeV due to capture on hydrogen is seen in the simulation, as well as a large number of events that deposit very little energy in the detector due to leakage. The broad response function to Gd captures is due to the fact that the shower spatial extent, defined by the typical 1–2 MeV energies of the gamma rays in the cascade, is of the order of the detector size. This means that only those interactions in the center of the detector will have a significant probability of depositing all of their energy in the detector. Interactions away from the detector center are likely to lose one or more gamma rays outside the detector volume, resulting in a lower visible energy deposition and accounting for the broad energy spectrum seen in the both the data and the simulation.

Table 1
Detection efficiency.

Quantity		Efficiency
Positron		$55 \pm 5\%$
Neutron		$40 \pm 4\%$
DAQ		$59 \pm 0.5\%$
-*Livetime*	$92 \pm 0.5\%$	
-*Muon veto*	$91 \pm 0.2\%$	
-$t_{min} = 10\ \mu s$	$70 \pm 0.5\%$	
Fiducial		$83 \pm 4\%$
Total		$10.7 \pm 1.5\%$

Based on the Monte Carlo, we estimate a detection efficiency of 40 % $\pm$ 4 % for antineutrino generated neutrons in the delayed energy region of 3.5 to 10 MeV.

8.6 Predicted Detection Efficiency

Aside from the prompt and delayed energy thresholds, the detection efficiency is also affected by the PMT asymmetry cut, the interevent and muon timing selection cuts and the deadtime of the DAQ. As described in Sec. 10, the interevent time distribution of antineutrino interactions is described by an exponential decay. We estimate the efficiency of this portion of our DAQ by integrating this exponential over the range of accepted interevent times (10–800 μsec). The fractional dead time imposed by the muon veto is given by the product of the 100 μs width veto with the sum of the trigger and muon rates (Sec. 7). Our means of estimating the fiducial volume of the detector, as defined by an analysis cut, is described in Sec. 10.2.

Table 1 shows the estimated efficiencies through each of our selection criteria, and the resulting total efficiency. It is interesting to note that even with the 40–50 % efficiency through the positron and neutron cuts, the underlying event rate is still high enough to give several hundred antineutrino events per day in our detector. When combined with the expected antineutrino interaction rate in our detector (Sec. 6) this efficiency allows us to estimate the number of antineutrino events that we should observe: 407 ± 75 /day.

9 Detector Calibration

Energy and time calibrations are performed periodically for each PMT-ADC pair and each TAC. The time scale is fixed by exercising each TAC with known fixed-interval start-and-stop pulses created by a pulse generator.

Relative calibration for each PMT-ADC pair and correction for long term drifts depends primarily on the interaction of the 2.6 MeV ^{208}Tl gamma ray from the Thorium chain with the detector. This gamma ray activity arises from the concrete walls and floor of the tendon gallery. Multiple Compton scatters of the gamma ray in the detector and surrounding material produce a broad spectral feature in the measured pulse height spectrum (Fig. 6).

The location of this feature, which is well fit by a gaussian, and the location of the electronic pedestal value (defined as the ADC channel measured for zero input voltage to the ADC) is automatically determined from each hour's data file. Since the signals from all cells are digitized when any one cell triggers, a large number of recorded events for a particular cell will have zero energy, i.e. will be a measurement of the energy pedestal (negligible electronic cross-talk is observed between PMTs). Calibration constants are applied for each PMT-ADC pair separately. The calibration procedure is as follows: determine the location of the energy pedestal; rebin the energy spectrum from 4000 channels to 800 channels; apply the PMT ratio cut described in Sec. 10 with a ratio of 0.1; fit the ^{208}Tl gamma ray feature to the sum of two exponentials and a Gaussian peak.

A more restrictive PMT ratio cut is used in the calibration procedure (0.1) than in the analysis used to extract candidate antineutrino events (0.4). While this means that the calibration samples only a subset ($\approx 70\%$) of the volume in which antineutrinos are counted, the subsequent improvement in energy resolution and gamma ray feature definition (Fig. 6) allow for a considerably more reliable determination of its position. This is a more important consideration for this detector, since we are more concerned with the stability of our analysis energy thresholds than with having a calibration that is averaged over the entire analyzed volume. Since we have no indication that the relative optical transport between the different volumes sampled by the calibration and the more general analysis has altered we are confident that it is consistent to apply this calibration to all events.

Once the ADC bin locations of both the pedestal and ^{208}Tl gamma ray feature are determined, an absolute calibration is imposed. The nominal energy of the ^{208}Tl gamma ray differs from the measured value in the detector due to energy leakage and other effects. To set the absolute energy scale, we performed a Monte Carlo simulation of gamma transport in the detector, as described

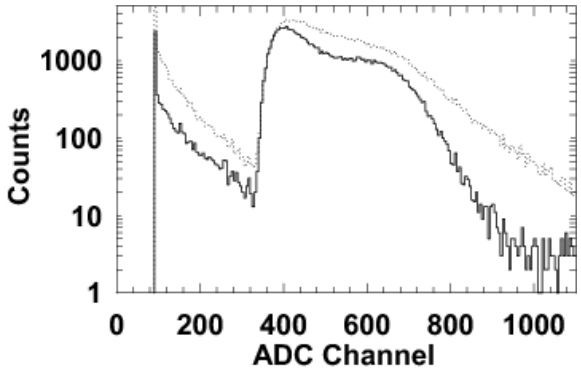

Fig. 6. A representative calibration spectrum from PMT 1, ADC 1 (solid). For comparison, the spectrum that results from accepting PMT ratios as great as 0.4 is also shown (dotted).

in Sec. 8. The location of the ^{208}Tl gamma ray feature is expected to be at 2.39 MeV. The error in this calibration procedure results in an error of $\approx$ 27 keV at 2.39 MeV and $\approx$ 40 keV at 3.5 MeV, which are the energy thresholds used in later analysis for prompt and delayed events, respectively. The calibrated PMT values for a cell are added to determine the energy of events in that cell in later analysis.

10 Antineutrino Event Selection

As described above, the 10 data items comprising an event are recorded whenever both PMTs attached to a single cell produce a signal exceeding the hardware thresholds. These are the ADC values for each of the 8 PMTs and both the time since the last acquisition trigger and the time since either the last acquisition trigger or the last muon veto hit, which ever is less. Events are streamed to disk soon after they are recorded.

Events are written to disk sequentially, with a new file created every hour. All analysis operations are performed on this unit of data. The product of this analysis is a reduced data set that can be combined across many hours, as the task at hand requires, and transmitted efficiently over a low bandwidth datalink for remote monitoring purposes.

10.1 Preliminary Analysis

As described in Sec. 4, we are looking for two energy depositions, arising from the positron and neutron interactions, in close time coincidence. The first step in the analysis is to form candidate event pairs from the raw singles data. For

every pair of sequential events, the first is labeled "prompt," or positron-like, and the second is labeled "delayed," or neutron-like. Two time intervals are also recorded: the time before the prompt event that the most recent muon veto or acquisition trigger occurred and the time between the prompt and delayed events (interevent time).

A complete hour of data taking typically comprises $\approx$ 1.4 million prompt/delayed pairs. Several items of interest are derived from this complete data set:

- the total number of acquisition triggers recorded in the hour,
- the interevent time spectrum of the entire data set is histogramed, and fit to an exponential to determine the acquisition trigger rate for that hour,
- the calibration constants for the PMT channels are determined as described in Sec. 9.

The next step in the analysis is to reduce the data set by applying an energy cut to the event pairs. To collect data for the automated calibration the discriminator thresholds are set well below the energy of the 2.6 MeV ^{208}Tl background line. However, as will be discussed below, the final antineutrino analysis thresholds must be set higher, since the background rate is too high at lower energies. Thus, a loose precut is made that requires greater than 2.0 MeV in both the prompt and delayed portions of an event, reducing the size of the data set that must be subsequently analysed by more than an order of magnitude.

10.2 Event Selection

To select antineutrino candidates we apply several further cuts.

In order to remove a strong position dependency in the light collection efficiency in our scintillator cells, a cut is applied to the ensure that each PMT in a cell sees a similar amount of light per event. An example of the light intensity seen by each PMT in a cell is shown in Fig. 7. Two clear features can be seen – a line along $PMT_A = PMT_B$, where an event occurs in the lower or middle portion of the cell so that the PMTs observe similar amounts of light, and large numbers of events on the "wings" where the light distribution is uneven. In those latter events the interaction point is closer to one PMT than the other resulting in uneven light collection, as well as a higher overall light collection efficiency that results in an incorrect energy assignment.

For this reason, we remove events with an uneven light distribution. This cut

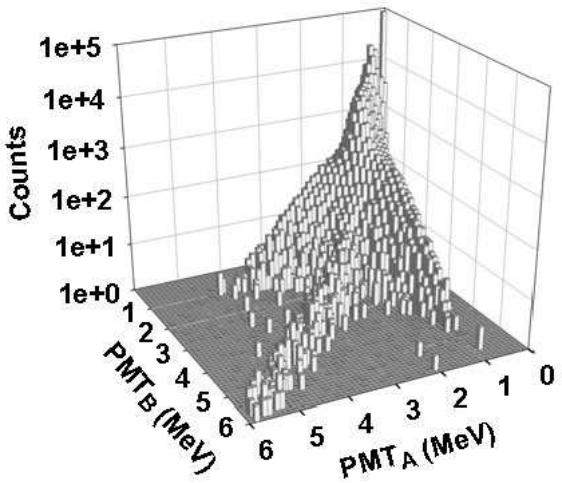

Fig. 7. Counts as a function of the share of energy in each PMT.

is applied to the normalized ratio of the two calibrated PMT intensities,

$$r = \left| \frac{PMT_A - PMT_B}{PMT_A + PMT_B} \right| < 0.4, \tag{4}$$

so that when the two PMTs observe similar intensity this quantity is small. The effect of this cut on the energy spectrum of singles in a cell is demonstrated in Fig. 8. Many events with apparent high energies are removed – in reality these are low energy singles that occur close to one PMT, yielding a higher light collection than events in the bulk of the scintillator cell. Thus, the effect of this cut is to exclude a volume close to the PMTs.

A GEANT4 [20] simulation was used to estimate the size of the remaining fiducial volume. Optical photons were generated throughout the cell volume, the number reaching each PMT recorded, and the PMT ratio cut applied. The simulation was repeating using several values for the scintillator attenuation length and cell wall reflectivity consistent with the LED scan shown in Fig. 4. The result was quite insensitive to these changes, and it is estimated that events in $83 \pm 4\%$ of the cell volume will pass this cut.

Next, we apply energy cuts to the amount of energy recorded in each cell. In this analysis we consider each scintillator cell to be an independent detector, i.e. we require that both the prompt and delayed energy distributions exceed an analysis threshold, and do not consider simultaneous energy depositions in any other cell. Because both the prompt and delayed energy depositions from an inverse beta interaction include gamma rays, energy can in fact be transported to adjacent scintillator cells, particularly for the delayed event (gamma ray shower following neutron capture on Gd). However, the energy sharing effect is relatively small – we have determined that considering the

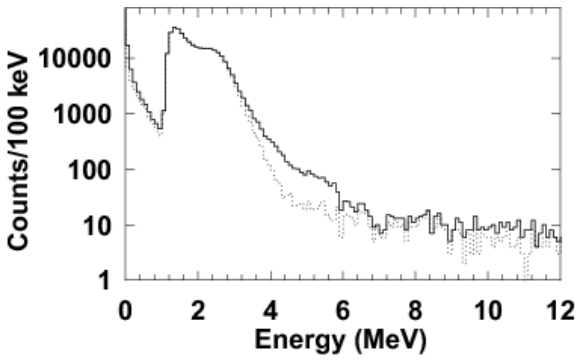

Fig. 8. The energy spectrum of a scintillator cell before (solid) and after (dotted) the PMT ratio cut is applied.

energy sum of all cells in the delayed energy determination would add only $\approx 10\%$ to the antineutrino count rate. This comes at the expense of increased complexity and that all scintillator cell/PMT combinations must be fully operational during the entire data taking period. For simplicity and flexibility in our analysis, we have chosen to consider each cell as an independent detector.

The lower energy thresholds for prompt and delayed events are optimized with respect to the long term stability of the threshold and the signal to background ratio. A lower threshold admits more of the desired antineutrino events but increases the number of uncorrelated background events, whose subtraction introduces considerable statistical uncertainty. In the two parameter space described by the prompt and delayed thresholds there is a fairly broad minimum in the statistical uncertainty in the number of correlated events. (Fig. 9). This gives us some freedom to choose thresholds values based on the stability criterion.

For the prompt event the lower threshold is set at the clearly identifiable 2.39 MeV calibration feature. This reduces the dependence of the analysis on the energy calibration, since no extrapolation of the energy scale from the measured calibration point is required. The delayed energy threshold is set at 3.5 MeV. With the prompt threshold set as just described, this value for the delayed threshold is optimized with respect to minimizing statistical uncertainty and maximizing the neutron detection efficiency.

Upper thresholds are chosen based on physical considerations. An upper threshold of 9 MeV is chosen for the prompt events since there are expected to be very few energy depositions due to reactor antineutrinos with energy greater than this (Sec. 8.4). For the delayed event, an upper threshold of 10 MeV is chosen, based on the expected delayed energy spectrum determined via Monte Carlo simulations (Sec. 8.5). This value reflects the maximum energy released by neutron capture on Gd, blurred by the energy resolution of the scintillator cells.

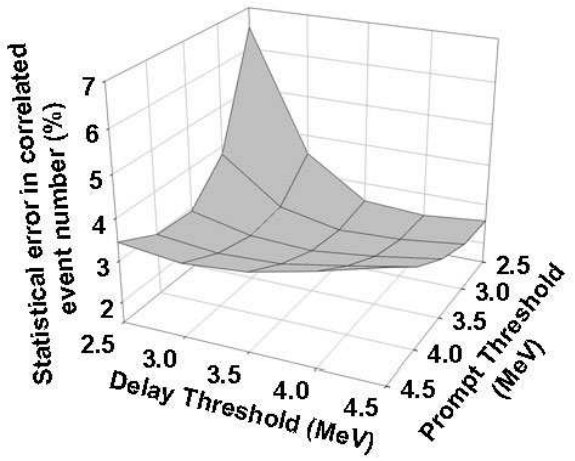

Fig. 9. The statistical uncertainty in the correlated event rate as a function of the prompt and delayed thresholds.

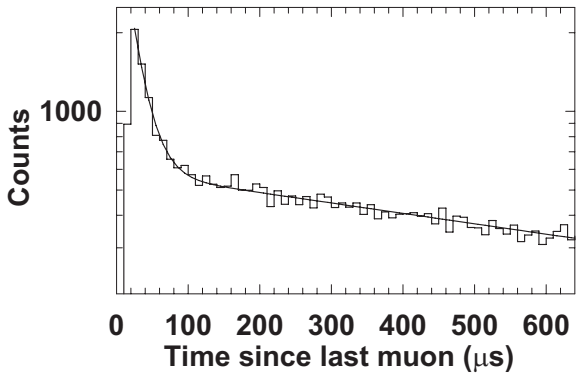

Fig. 10. Measured values of the time elapsed since the last muon or cell event.

Finally, we apply a cut that suppresses antineutrino-like event pairs caused by muon interactions. Fig. 10 displays the spectrum of time since the last muon or acquisition trigger values once all the cuts described above have been applied. As expected for a Poisson process, the dominant feature is a simple exponential with time constant equal to inverse the rate at which events occur, in this case the sum of the muon veto hit rate and the acquisition trigger rate. At shorter times there are additional events that are correlated with muon hits in the veto – it is these that we must be careful to eliminate. For this reason we apply a cut on this value, considering only those events that occur at least 100 μs after the last muon hit/acquisition trigger. From the measured time constant of the muon correlated events (20 μs), we calculate that this cut excludes all but 0.7% of events correlated with a muon recorded in the veto.

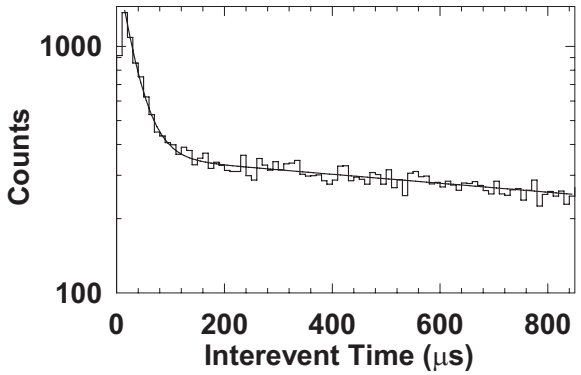

Fig. 11. A representative interevent time spectrum of event pairs that pass all selection cuts acquired during 7 days of data taking.

10.3 Antineutrino count rate determination

After applying these cuts, we then examine the interevent time spectrum (Fig. 11). Two clear exponential features are visible. The first and most interesting is that due to correlated pairs of events, a positron-like energy deposition followed a characteristic time later by the capture of a neutron on a Gd nucleus. The second exponential is that due to random coincidences of sequential background events that both exceed the relevant thresholds. As would be expected for such event pairs, the time constant of this exponential is equal to the acquisition trigger rate.

Because it is impossible in this detector to distinguish random coincidences from true correlated event pairs on an event-by-event basis, we use a statistical separation of the two to determine the correlated (antineutrino-like) event rate. This is achieved by fitting the spectrum displayed in Fig. 11 to the sum of two exponentials. The two time constants are known in advance; the uncorrelated rate is measured from the raw data, and the neutron capture time constant is measured from a high statistics data set (28.6 ± 0.3 μs). Thus, we need only fit for two parameters, the amplitude of each exponential. Simple integrals,

$$N = A \int_{10\ \mu s}^{800\ \mu s} e^{-t/\tau}\, dt, \tag{5}$$

then yield the number of event pairs that fall into each class. The fit is implemented using the CERN MINUIT package [21], using full error propagation, so that bin-to-bin statistical errors are correctly applied in determining the best fit exponential amplitudes and their uncertainties.

The energy spectra of the prompt and delayed portions of correlated events can also be extracted using a statistical separation – this is again necessary

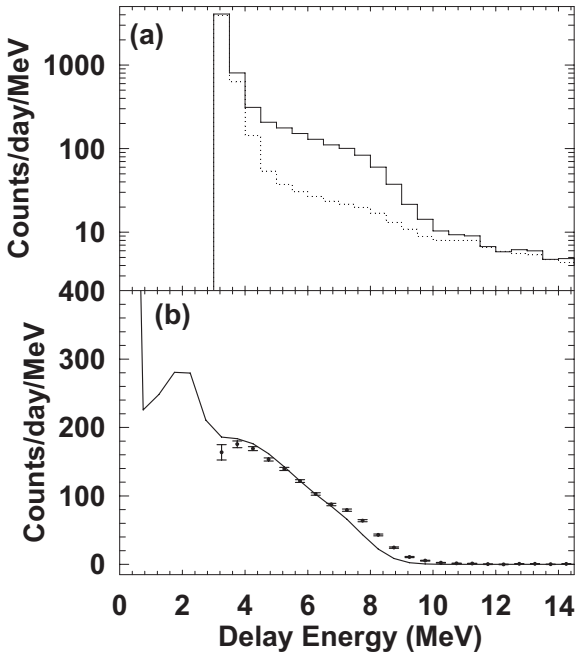

Fig. 12. Energy spectra of correlated events (delayed in this example) are obtained using a statistical separation. (a) The average energy spectrum of uncorrelated events is determined using events with long interevent time (dotted) and is then subtracted from spectra determined at short interevent times (solid). This yields the average energy spectrum of the correlated events (b). The solid line shows the neutron energy spectrum predicted by the Monte Carlo, including the expected feature at ≈ 2.2 MeV due to capture on hydrogen.

due to our inability to distinguish correlated and uncorrelated events on an event-by-event basis. The procedure used is demonstrated for the delayed case in Fig. 12. The average energy spectra for uncorrelated events are determined from events with long interevent times ($400 - 800$ μs), while the sum of the average energy spectra for correlated and uncorrelated events is determined from those with short interevent times ($10 - 100$ μs). The uncorrelated spectra are scaled so that there are equal numbers of uncorrelated events in both the short and long time energy spectra, and are then subtracted from the short time spectra, yielding the average correlated energy spectra.

11 Confirmation of Reactor Antineutrino Detection

Having extracted the number of correlated events, we then wish to determine what fraction of those are due to antineutrino interactions. Unfortunately we have no means to distinguish these from correlated backgrounds, such as those caused by fast neutrons. Instead, we must wait for the antineutrino source, the SONGS Unit 2 reactor, to turn off. This occurs approximately every 1.5 years during regularly scheduled refueling outages, as well as occasionally for inspec-

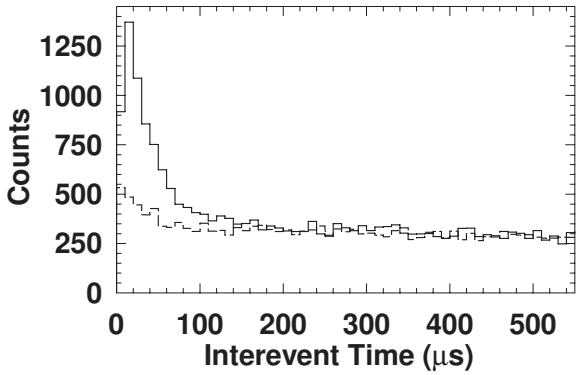

Fig. 13. Interevent time spectra acquired over 7 days with the Unit 2 reactor off (dashed) and on (solid).

Table 2
Comparison of measurements with the Unit 2 reactor on and off.

Reactor State	Off	On
Uncorrelated Events	3732 ± 25 /day	3785 ± 26 /day
Correlated Events	105 ± 9 /day	564 ± 13 /day
DAQ trigger rate	420 ± 1 Hz	418 ± 1 Hz
Muon veto rate	506 ± 1 Hz	503 ± 1 Hz

tions or brief unscheduled maintenance operations. With the Unit 2 reactor off the detector counts correlated background events and a small number of antineutrino interactions from the relatively distant Unit 3.

Fig. 13 displays the interevent time spectra for two 7 day periods in April and May of 2006. In the first period, Unit 2 was at zero power for refueling. During this time around 100 correlated events pass all selection cuts. In the second, refueling was completed and the reactor was operating at full power.

Clearly, there are many more correlated events when the reactor is on, compared to when the reactor is off. Also, the uncorrelated portion of the interevent time spectrum is unaltered by the change in reactor state, as are the detector trigger and muon veto rate. The number of correlated and uncorrelated events contained in the two spectra is compared in Table 2. The reactor off measurement is essentially a measurement of the correlated background rate. It comprises less than 20% of the correlated event rate, giving good signal to noise for a measurement of the reactor antineutrino rate. The 7 day average of the observed antineutrino detection rate, 459 ± 16 /day, is in good agreement with that predicted, 407 ± 75 /day.

To further confirm that we are observing reactor antineutrinos, we can also examine the prompt event energy spectrum during reactor on and off periods (Fig. 14a). With the Unit 2 reactor off, we are measuring the prompt energy

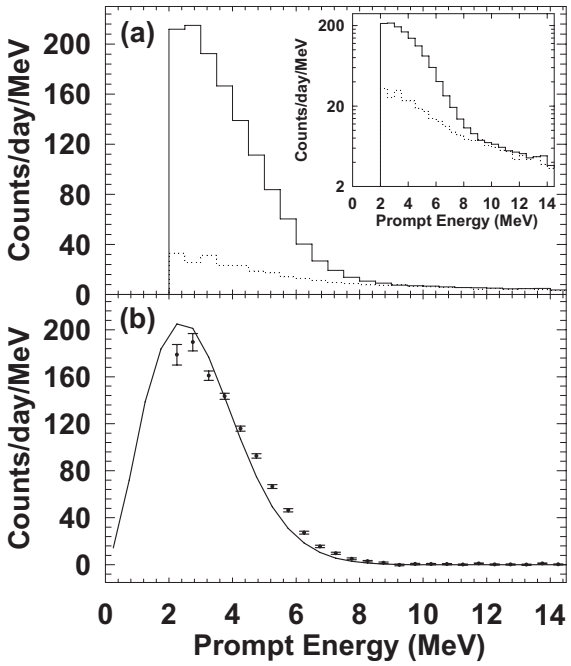

Fig. 14. (a) The energy spectrum of prompt correlated events with the Unit 2 reactor on (solid) and off (dotted). The logarithmic insert clearly shows the agreement between the two spectra at energies greater than 9 MeV. (b) The inferred inverse beta positron energy spectrum derived by subtracting the reactor off data from the reactor on data. The solid line shows the Monte Carlo prediction, including transport effects and the simple optical model.

spectrum of the correlated backgrounds, while with the reactor on we measure the sum of these backgrounds and the prompt antineutrino interaction energy deposition.

As discussed in Sec. 4 the prompt energy deposition in an inverse beta interaction is essentially that of the incoming antineutrino. The expected prompt energy spectrum was given in Sec. 8.4; we expect the distribution to go to zero at around 10 MeV. This is what we observe in Fig. 14a – above this energy the reactor on and reactor off distributions agree.

Furthermore, we can determine the prompt energy spectrum of the reactor correlated events (Fig. 14b), and compare it to that expected from the Monte Carlo calculation (Sec. 8.4). The agreement is good, again confirming that we are indeed detecting reactor antineutrinos.

In principle, the highest energy neutrons in the reactor spectrum could create a correlated antineutrino-like signal in the detector in that same way that fast neutrons produced by cosmic rays do. However, as noted in Sec. 3, this rate is negligible, since reactor fast and thermal neutrons from the core are completely attenuated by the ≈ 20 m of concrete between the core and the detector. The reactor associated gamma flux at the detector location is similarly negligible.

12 Conclusion

Our deployment of an antineutrino detector at a nuclear reactor has shown that even a cubic meter scale detector of modest efficiency can easily measure hundreds of antineutrino events per day, a large enough count rate to be of interest for cooperative monitoring regimes. Of particular interest is the relative smallness of the detector compared to many other modern reactor antineutrino detectors. (These earlier detectors have typically used larger active volumes to improve containment of the spatially diffuse neutron-induced gamma shower, while we have sacrificed some efficiency to reduce our overall footprint.) We have also shown that the detector can operate for months to years with only very occasional maintenance needed by the safeguards inspector. This is an important point since inspector-days dominate the cost of reactor safeguards regimes. Calibrations can be performed using omnipresent gamma ray backgrounds, without the need for external check sources. Concerning stability of response, we have been able to use scintillator mixed several years prior to our experiment, for two years running, with no observable reduction in response due to aging. This perhaps surprising result again relates to the smallness of our detector, where the typical travel paths for scintillation photons are only of the order 1-2 meters compared to several meters or tens of meters in other experiments. Our impact on day-to-day operations at the reactor site has been negligible, an important consideration for gaining acceptance by reactor operators. As far as the deployment site itself is concerned, as noted above in Sec. 3, we are gratified to have found that many reactors around the world appear to possess annular galleries with overburden and standoff characteristics similar to the ones enjoyed in our own installation.

In summary, our initial experience with deployment augurs well for the near-term utility of this novel reactor safeguards tool. Shortly, we will also publish analyses of our current data set quantifying the precision with which thermal power and fissile content can be measured with the SONGS1 design.

Acknowledgements

We thank DOE NA-22 for their continued support of this project. We are indebted to the management and staff of the San Onofre Nuclear Generating Station for site access and the excellent support they have provided us. N. Madden, D. Carr, J. Gollnick, and A. Salmi made essential contributions to the electronic and mechanical design and construction of the detector. We thank D. McNabb for assistance with "dicebox" calculations. We are particularly grateful to F. Boehm for providing us with the liquid scintillator used in this detector. We gratefully acknowledge useful discussions with R. Svoboda

and S. Dazeley.

References

[1] Yu. V. Klimov, et. al., Atomic Energy, 76 (1994) 123

[2] A. Bernstein, et. al., J. Appl. Phys. 91 (2002) 4672

[3] www.iaea.org/Publications/Factsheets/English/S1_Safeguards.pdf

[4] Vogel, P., et. al., Phys. Rev. C 24 (1981) 1543

[5] V. N. Shah, et. al., Nucl. Eng. Des. 185 (1998) 51

[6] B. Barbe, et. al., Nucl. Eng. Des. 125 (1991) 57

[7] K. Alex, et. al., Transactions of the 16th International Conference on Structural Mechanics in Reactor Technology, (2001) 1715

[8] M. Grey, et. al., Transactions of the 16th International Conference on Structural Mechanics in Reactor Technology, (2001) 1811

[9] N. K. Prinja, et. al., Transactions of the 17th International Conference on Structural Mechanics in Reactor Technology, (2003) H04-6

[10] S. Miyake, Proceedings of the International Cosmic Ray Conference, 5, (1973) 3638

[11] P. Vogel and J. F. Beacom, Phys. Rev. D 60 (1999) 053003

[12] J. Delorme, et. al., Phys. Rev. C 52 (1995) 2222

[13] F. Boehm, et. al., Phys. Rev. D 62 (2000) 092005

[14] V. Chazal, et. al., Nucl. Instr. and Meth. A. 490 (2002) 334

[15] M. Abbes, et. al., Nucl. Instr. and Meth. A. 374 (1996) 164

[16] F. Boehm, et. al., Phys. Rev. D 64 (2001) 112001

[17] A. G. Piepke, et. al., Nucl. Instr. and Meth. A. 432 (1999) 392

[18] MCNPX User's Manual, v. 2.5.0, D. Pelowitz, ed., LA-CP-05-0369 (2005)

[19] F. Becvar, Nucl. Instr. and Meth. A., 417 (1998) 434

[20] S. Agostinelli, et. al., Nucl. Instr. and Meth. A. 506 (2003) 250

[21] F. James, CERN Program Library Long Writeup D506